deformable particle packings in periodic boundary conditions given that deformable particles possess spherical vertices on their surfaces and provide expressions for the components of the stress tensor in systems with periodic boundary conditions given that the shape-energy function of deformable particles includes many-body potentials. We will use these results to show the pressure versus packing fraction relation near jamming onset for packings of deformable particles in 2D. We also compare the vibrational density of states of jammed packings of floppy particles, elastic shells, and surface-energy dominated particles with rough interactions in 2D and 3D, by calculating the eigenvalue spectrum of the dynamical matrix.

A. Calculation of Packing Fraction

The packing fraction ϕ plays a dominant role in controlling the collective mechanical properties of many particulate systems. We will focus on systems near jamming onset, where overlaps between deformable particles are small compared to the particle size. In this case, the packing fraction is the total area (volume) occupied by the particles divided by the area (volume) of the confining boundaries. The area (volume) of each particle is determined by the edges of the particle that define the interaction potential between particles in Eq. 3 for rough particles and Eq. 5 for smooth particles. In this subsection, we describe the calculation of the packing fraction ϕ for collections of N rough deformable particles in a square box with side length L in 2D with periodic boundary conditions and validate the method using Monte-Carlo integration. Calculations of ϕ for deformable particles with smooth interactions and in 3D can be obtained using similar methods.

The area occupied by a collection of 2D deformable particles with rough interactions is the sum of the areas of the polygons and vertices for each particle. (See Fig. 8 (a).) However, we must subtract off the areas of regions that are double-counted for overlaps that occur between two vertices on a given particle, overlaps between the vertices and polygon on a given particle, as well as overlaps between vertices on different particles. If the vertices on a given deformable particle do not overlap significantly, $0.1 < r_{\mu i,\mu j}/\sigma_\mu < 1$, we only need to consider overlaps between pairs of vertices and a single vertex overlap with each polygon. The area of a collection of deformable particles is

$$A_{\rm particles} = A_{\rm polygon} + A_{\rm vertices} - A_{\rm sector} - A_{\rm pair}, \tag{19}$$

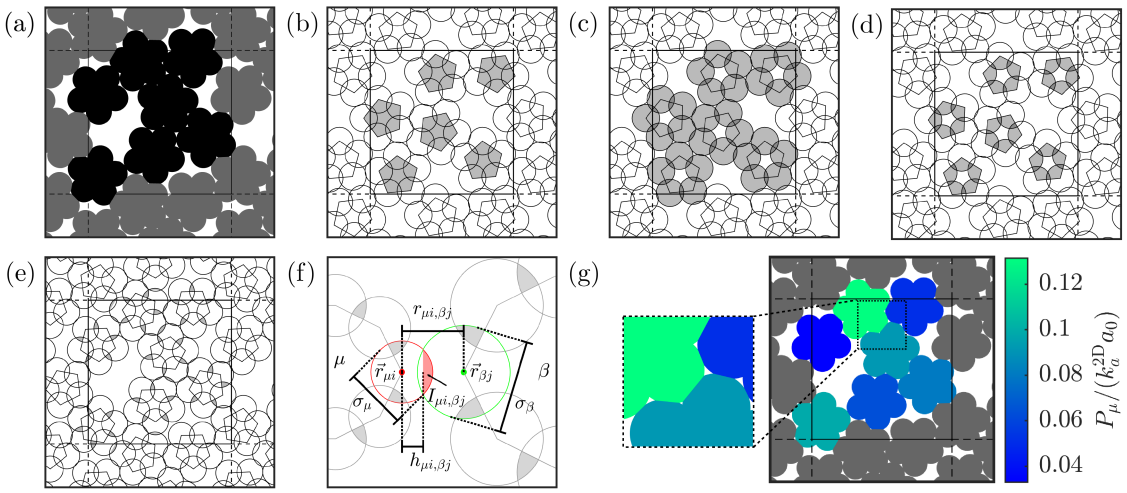

FIG. 8. (a) A jammed packing of $N = 7$ rough, deformable particles. We show the area of the particles $A_{\text{particles}}$ in the main simulation cell (black), unoccupied area (white), and area of particles in the image cells (gray). The packing fraction ϕ is the ratio of the area in black to the total area of the main cell. The area of the particles has four contributions: $A_{\text{particles}} = A_{\text{polygon}} + A_{\text{vertices}} - A_{\text{sector}} - A_{\text{pair}}$. (b) A_{polygon} is shaded gray. (c) The area of the vertices in the main cell A_{vertices} is shaded grey. (d) The regions A_{sector} that are counted both in the polygon and vertex areas are shaded gray. (e) The vertex-vertex overlaps outside of the particle polygons A_{pair} are shaded gray. (f) A close-up of vertex i (red) on particle μ overlapping with vertex j (green) on particle β. σ_μ and σ_β are the diameters of the vertices, $r_{\mu i,\beta j}$ is their separation, and $h_{\mu i,\beta j}$ is the distance from $\vec{r}_{\mu i}$ to the planar interface with vertex j on particle β. $I_{\mu i,\beta j}$ is the red-shaded area. Intraparticle vertex-vertex overlaps outside of the particle polygons are shown in gray; these regions correspond to the first term in Eq. 20. (g) Each particle area A_μ is shaded according to the local pressure $P_\mu = \text{Tr}(\overline{\Sigma}_\mu)/2$ (in units of $k_a^{2D}a_0$, where a_0 is the average preferred area). The close-up shows the planar interfaces between several vertices on different particles. In (a)-(e), and (g), the main cell is indicated by a solid black line, and the image cells are indicated by dashed black lines.

where $A_{\text{polygon}} = \sum_{\mu=1}^{N} a_\mu$, is the area of the polygon for each particle. (See Fig. 8 (b).) The total area of the vertices for all particles is $A_{\text{vertices}} = \sum_{\mu=1}^{N}\sum_{i=1}^{N_\mu} \pi\sigma_\mu^2/4$. (See Fig. 8 (c).) $A_{\text{sector}} = \sum_{\mu=1}^{N}\sum_{i=1}^{N_\mu} \sigma_\mu^2(\pi - \theta_{\mu i})/8$ is the area of the overlaps between each vertex and the polygon of the particle to which they belong, as shown in Fig. 8 (d). The area of the

overlaps between the vertices that occur outside of the particle polygons is

$$A_{\rm pair} = \sum_{\mu=1}^{N}\sum_{i=1}^{N_\mu} I_{\mu i,\mu(i+1)} + \sum_{\mu=1}^{N}\sum_{i=1}^{N_\mu}\sum_{\substack{\beta=1\\ \beta\neq\mu}}^{N}\sum_{j=1}^{N_\beta} I_{\mu i,\beta j}, \tag{20}$$

which includes both intra- and inter-particle vertex-vertex overlaps and is shaded gray in Fig. 8 (e). In Eq. 20, $I_{\mu i,\beta j}$ is the area of one of the two circular segments (with radius $\sigma_\mu/2$) defined by the points where overlapping vertices i on particle μ and j on particle β intersect [43]. The area of overlap between vertex i on particle μ and vertex j on particle β is

$$\begin{aligned} I_{\mu i,\beta j} =& \Theta(\sigma_{\mu\beta} - r_{\mu i,\beta j})\Bigg[\left(\frac{\sigma_\mu}{2}\right)^2 \arccos\left(\frac{r_{\mu\beta}^2 - \left(\frac{\sigma_\beta}{2}\right)^2 + \left(\frac{\sigma_\mu}{2}\right)^2}{\sigma_\mu r_{\mu\beta}}\right) \\ & - \frac{r_{\mu\beta}^2 - \left(\frac{\sigma_\beta}{2}\right)^2 + \left(\frac{\sigma_\mu}{2}\right)^2}{2r_{\mu\beta}}\sqrt{\left(\frac{\sigma_\mu}{2}\right)^2 - \left(\frac{r_{\mu\beta}^2 - \left(\frac{\sigma_\beta}{2}\right)^2 + \left(\frac{\sigma_\mu}{2}\right)^2}{2r_{\mu\beta}}\right)^2}\Bigg]. \end{aligned} \tag{21}$$

The first term in the square brackets is the area of the circular sector defined by vertex i and the intersection points with vertex j, and the second term removes the area of the triangle defined by the intersection points and $\vec{r}_{\mu i}$. The Heaviside function ensures that $I_{\mu i,\beta j}$ only contributes to $A_{\rm pair}$ when vertex i and j overlap. (See the red-shaded region in Fig. 8 (f).) In Eq. 20, the first term is a sum over adjacent vertices in each particle, and since all vertices on particle μ have the same diameter, $I_{\mu i,\mu(i+1)}$ is half the overlap between vertex i and vertex $i+1$. We only use this half overlap when calculating $A_{\rm pair}$ because only half of the intersection occurs outside the polygon of particle μ. In the second term in Eq. 20, the double sum $\sum_{\beta=1,\beta\neq\mu}^{N}\sum_{j=1}^{N_\beta} I_{\mu i,\beta j}$ is the size of the double-counted region we associate with vertex i on particle μ from overlaps with vertices on other particles. Thus, the area attributed to a single deformable particle μ is

$$A_\mu = a_\mu + \sum_{i=1}^{N_\mu}\frac{\pi}{4}\sigma_\mu^2 - \sum_{i=1}^{N_\mu}\sigma_\mu^2\frac{(\pi-\theta_{\mu i})}{8} - \sum_{i=1}^{N_\mu} I_{\mu i,\mu(i+1)} - \sum_{i=1}^{N_\mu}\sum_{\substack{\beta=1\\ \beta\neq\mu}}^{N}\sum_{j=1}^{N_\beta} I_{\mu i,\beta j}. \tag{22}$$

While it is possible to make other choices concerning the attribution of double-counted area between vertices on different particles, this choice reflects the idea that the particles deform such that that two contacting vertices form a planar interface, and as a result the area

occupied by vertex i should be reduced by $I_{\mu i,\beta j}$. In Fig. 8 (g), the blue- and green-shaded regions indicate A_μ (Eq. 22) for each particle.

Using Eq. 19, the packing fraction is defined as

$$\phi = A_{\text{particles}}/L^2. \tag{23}$$

In Table II, we compare the analytic expressions for ϕ and the four contributions to $A_{\text{particles}}$ (i.e. A_{polygon}, A_{vertices}, A_{sector}, and A_{pair}) to those found using Monte-Carlo integration for the deformable particle packing in Fig. 8 (a). For example, we find $\phi = 0.8397$ using Eq. 23 and $\phi = 0.8391 \pm 0.0008$ using Monte-Carlo integration for this deformable particle packing. The packing in Fig. 8 (a) contains elastic shell particles with $k_l^{2D}/k_c = 2$, $k_b^{2D}/(k_c\sigma^2) = 0.3$, and $k_a^{2D}a_0^2/(k_c\sigma^2) = 0.9$ with rough interactions, $N_\mu = 5$, $N = 7$, and $\mathcal{A}_0^{2D} = \mathcal{A}_{\text{min}}$.

Method	$\phi = A_{\text{particles}}/L^2$	A_{polygon}/L^2	A_{vertex}/L^2	A_{sector}/L^2	A_{pair}/L^2
Analytic	0.8397	0.276	0.8648	0.259	0.0415
Monte Carlo	0.8391 ± 0.0008	0.276 ± 0.001	0.8642 ± 0.0008	0.260 ± 0.001	0.0410 ± 0.0004

TABLE II. The packing fraction $\phi = A_{\text{particles}}/L^2$ and the four contributions to $A_{\text{particles}} = A_{\text{polygon}} + A_{\text{vertices}} - A_{\text{sector}} - A_{\text{pair}}$ (Eq. 19) for the deformable particle packing in Fig. 8. For ϕ and each area contribution, we compare the analytical expressions in the middle row to those obtained from Monte-Carlo integration in the bottom row. The errors in the Monte-Carlo integration scale as $\sim N_m^{-1/2}$, where N_m is the number of Monte-Carlo trials.

B. Stress Tensor for Deformable Particles in Periodic Boundary Conditions

The stress tensor $\overline{\Sigma}$ of a jammed packing of deformable particles describes the mechanical response of the packing. The stress tensor is symmetric with $d(d+1)/2$ independent components in d dimensions. The pressure is given by the diagonal elements of the stress tensor, $P = \text{Tr}(\overline{\Sigma})/d$, where Tr is the trace. The off-diagonal components of the stress tensor give the shear stress. The stress tensor is straightforward to calculate for systems of point particles with fixed-wall boundary conditions. For periodic boundary conditions, the potential energy (and thus the stress tensor) has an additional dependence on the length of the boundary from the minimum image convention [44]. For systems with *only* pairwise, central potentials, the additional dependence on box length can be captured by summing over

each pair interaction and using the main simulation cell position of one particle in the pair and the closest image position of the other particle when calculating each pair interaction's contribution to the stress tensor [45]. The shape-energy function for deformable particles includes not only pair interactions, but also many-body potentials. (See Eqs. 1 and 2.) In this section, we will first review expressions for the stress tensor for collections of particles that interact via repulsive pairwise, central potentials with periodic boundary conditions. We then generalize the expressions for the stress tensor for packings of deformable particles to include many-body interactions with periodic boundary conditions. We also discuss a method for defining the stress tensor for each particle that sums to the total stress tensor when averaged over all particles in the system. Using these relations for the stress tensor, we calculate the pressure of deformable particle packings as a function of packing fraction as they are isotropically compressed above jamming onset.

For a 2D system of N elastic disks modeled by point particles with short-range pairwise, central potentials and fixed-wall boundary conditions, the stress tensor can be defined as

$$\overline{\Sigma}_{ab} = \left\langle \frac{1}{A_{\text{system}}} \sum_{n=1}^{N} \left(m_n v_{n,a} v_{n,b} + r_{n,a} F_{n,b} \right) \right\rangle, \tag{24}$$

where a, $b = x$, y, $r_{n,a}$ and $v_{n,a}$ are the ath components of the position and velocity vectors for disk n, and m_n is the mass of disk n. $F_{n,b}$ is the bth component of the net force on disk n, A_{system} is the area of the system, and $\langle \cdot \rangle$ gives the ensemble average. In Eq. 24, the first term is the contribution to the stress tensor from momentum transfer through particle motion, while the second term is the force moment or virial contribution.

However, Eq. 24 does not hold for systems with periodic boundary conditions [45]. The stress tensor can be calculated for systems with pairwise interactions in periodic boundary conditions by making a specific choice for the position factor in the force moment. When calculating the contribution to the stress tensor for the pair interaction between disk n and disk m, we use the position of disk n in the main simulation cell, and the closest image position of disk m, since these are the positions used to calculate the interaction potential and forces between disks n and m within the main simulation cell [44]. Using this method,

$$\overline{\Sigma}_{ab} = \left\langle \frac{1}{A_{\text{system}}} \left(\sum_{n=1}^{N} m_n v_{n,a} v_{n,b} + \sum_{n=1}^{N-1} \sum_{m=n+1}^{N} \left(r_{n,a}^{n,\text{pair}} F_{nm,b}^{n,\text{pair}} + r_{m,a}^{n,\text{pair}} F_{mn,b}^{n,\text{pair}} \right) \right) \right\rangle, \tag{25}$$

where $r_{n,a}^{n,\text{pair}}$ is ath component of the position vector of disk n in the main simulation cell and $r_{m,a}^{n,\text{pair}}$ is the ath component of the position vector of the closest image of disk m to disk

n. $F^{n,\text{pair}}_{nm,b} = -\frac{\partial}{\partial r^{n,\text{pair}}_{n,b}} U^{\text{pair}}_{nm}$ is the bth component of the force on disk n from the pair force on disk n from disk m and $F^{n,\text{pair}}_{mn,b} = -\frac{\partial}{\partial r^{n,\text{pair}}_{m,b}} U^{\text{pair}}_{nm}$ is the bth component of the pair force on disk m from disk n. U^{pair}_{nm} is the pair potential between disks n and m using the minimum image distance between them. Eq. 25 can then be rearranged as

$$\overline{\Sigma}_{ab} = \left\langle \frac{1}{A_{\text{system}}} \left(\sum_{n=1}^{N} m_n v_{n,a} v_{n,b} - \sum_{n=1}^{N-1} \sum_{m=n+1}^{N} r^{n,\text{pair}}_{nm,a} F^{\text{pair}}_{nm,b} \right) \right\rangle, \tag{26}$$

where $r^{n,\text{pair}}_{nm,a} = r^{n,\text{pair}}_{m,a} - r^{n,\text{pair}}_{n,a}$, using Newton's third law.

In the case of deformable particles, the total potential energy (and therefore the stress tensor) has two contributions. First, the total potential energy includes pairwise interactions from vertices on different particles, which can be treated using Eq. 26. The second contribution includes many-body interactions from the shape-energy function $U^{\text{2D}}_{\mu,\text{shape}}$. How do the many-body interactions contribute to the stress tensor for systems with periodic boundary conditions? We calculate the stress tensor using the copy of each particle whose center of mass occurs in the main simulation cell. We use the positions of these copies when calculating the shape-energy contribution to the force moment. This choice ensures, as required, that the contributions from the shape-energy function for each particle appear only once in the stress tensor and that the positions used to calculate the force moment correspond to those used to calculate the shape-energy functions [44]. The stress tensor of a system of N deformable particles is

$$\begin{aligned} \overline{\Sigma}_{ab} = \Bigg\langle \frac{1}{A_{\text{system}}} \Bigg(& \sum_{\mu=1}^{N} \sum_{i=1}^{N_\mu} \left(m_{\mu i} v_{\mu i,a} v_{\mu i,b} + \tilde{r}_{\mu i,a} F^{\text{shape}}_{\mu i,b} \right) \\ & - \sum_{\mu=1}^{N-1} \sum_{i=1}^{N_\mu} \sum_{\beta=\mu+1}^{N} \sum_{j=1}^{N_\beta} r_{\mu i,\beta j,a} F^{\text{rough}}_{\mu i,\beta j,b} \Bigg) \Bigg\rangle, \end{aligned} \tag{27}$$

where $m_{\mu i}$ is the mass of vertex i on paritcle μ and $v_{\mu i,a}$ is the ath component of the velocity vector of vertex i on particle μ. $\tilde{r}_{\mu i,a}$ is the ath component of the position vector of vertex i on the copy of particle μ that appears in the main simulation cell. The first term in the double sum is the contribution to the stress tensor from momentum transport via particle motion. The second term is the contribution from the shape-energy function, where $F^{\text{shape}}_{\mu i,b} = -\frac{\partial}{\partial \tilde{r}_{\mu i,b}} U^{\text{2D}}_{\mu,\text{shape}}$ is the bth component of the net force on vertex i of particle μ arising from shape-energy forces. The quadruple sum is the contribution from each vertex-vertex pair interaction $U^{\text{rough}}_{\mu i,\beta j}$, where $r_{\mu i,\beta j,b}$ is the bth component of the separation vector between

vertex i on particle μ in the main simulation cell and the closest image of vertex j on particle β and $F^{\text{rough}}_{\mu i,\beta j,b} = -\frac{\partial}{\partial r_{\mu i,b}} U^{\text{rough}}_{\mu i,\beta j,a}$ is the bth component of the pair force on vertex i on particle μ from vertex j on β.

A similar formulation for the stress tensor can be developed for smooth interactions between deformable particles in systems with periodic boundary conditions. In this case, the quadruple sum in Eq. 27 is replaced with three quadruple sums that account for the forces arising from $U^{\text{edge}}_{\mu i,\beta j}$, $U^{\text{concave}}_{\mu i,\beta j}$, and $U^{\text{convex}}_{\mu i,\beta j}$. We use the position of particle β in the main simulation cell given by $\tilde{r}_{\beta j}$ and the closest image of $\vec{r}_{\mu i}$ in Eqs. 6, 9, and 10.

In static packings of deformable particles in systems with periodic boundary conditions, we can also quantify the stress tensor for each particle μ:

$$\overline{\Sigma}_{\mu,ab} = \left\langle \frac{1}{A_\mu} \left(\sum_{i=1}^{N_\mu} \tilde{r}_{\mu i,a} F^{\text{shape}}_{\mu i,b} - \sum_{i=1}^{N_\mu} \sum_{\substack{\beta=1 \\ \beta \neq \mu}}^{N} \sum_{j=1}^{N_\beta} \frac{h_{\mu i,\beta j}}{r_{\mu i,\beta j}} r_{\mu i,\beta j,a} F^{\text{rough}}_{\mu i,\beta j,b} \right) \right\rangle, \tag{28}$$

where A_μ is the area of particle μ in Eq. 22 and $h_{\mu i,\beta j}$ is the distance from vertex i on particle μ to the 'contact line' with vertex j on particle β as shown in Fig. 8 (f). The triple sum allocates a fraction of the force moment arising from the interaction between vertex i on particle μ and vertex j on particle β to particle μ that is proportional to $h_{\mu i,\beta j}/r_{\mu i,\beta j}$, which is the fraction of the separation vector $\vec{r}_{\mu i,\beta j}$ that lies within A_μ [46, 47]. (See Fig. 8 (f) and (g).)

We emphasize that for this definition of the local stress tensor we assumed that the stresses arising from the shape-energy function occur within the area spanned by the deformable particle. We also *chose* to distribute the contact stresses along the shortest line between contacting vertices and use the Irving-Kirkwood convention [48] of assuming that stress from a pair interaction acts along the line between the two points. However, other definitions of local stresses are also valid [49]. In Fig. 8 (g), we show that the local pressure $P_\mu = \text{Tr}\left(\overline{\Sigma}_\mu\right)/2$ on each particle varies in static packings of elastic shell particles ($k_l^{2\text{D}}/k_c = 2$, $k_b^{2\text{D}}/k_c = 0.3$, and $k_a^{2\text{D}}/k_c = 0.9$) with rough interactions, $N_\mu = 5$, $N = 7$, and $\mathcal{A}_0^{2\text{D}} = \mathcal{A}_{\text{min}}^{2\text{D}}$. The total stress tensor of the system can be obtained by calculating the area-weighted sum of the single particle stress tensors over all particles: $\overline{\Sigma} = \sum_{\mu=1}^{N} A_\mu \overline{\Sigma}_\mu / A_{\text{system}}$.

Obtaining the pressure P and packing fraction ϕ of static packings of deformable particles is crucial to understanding their mechanical properties. For instance, in mechanically stable, amorphous packings of soft, bidisperse disks in 2D that interact via purely repulsive linear

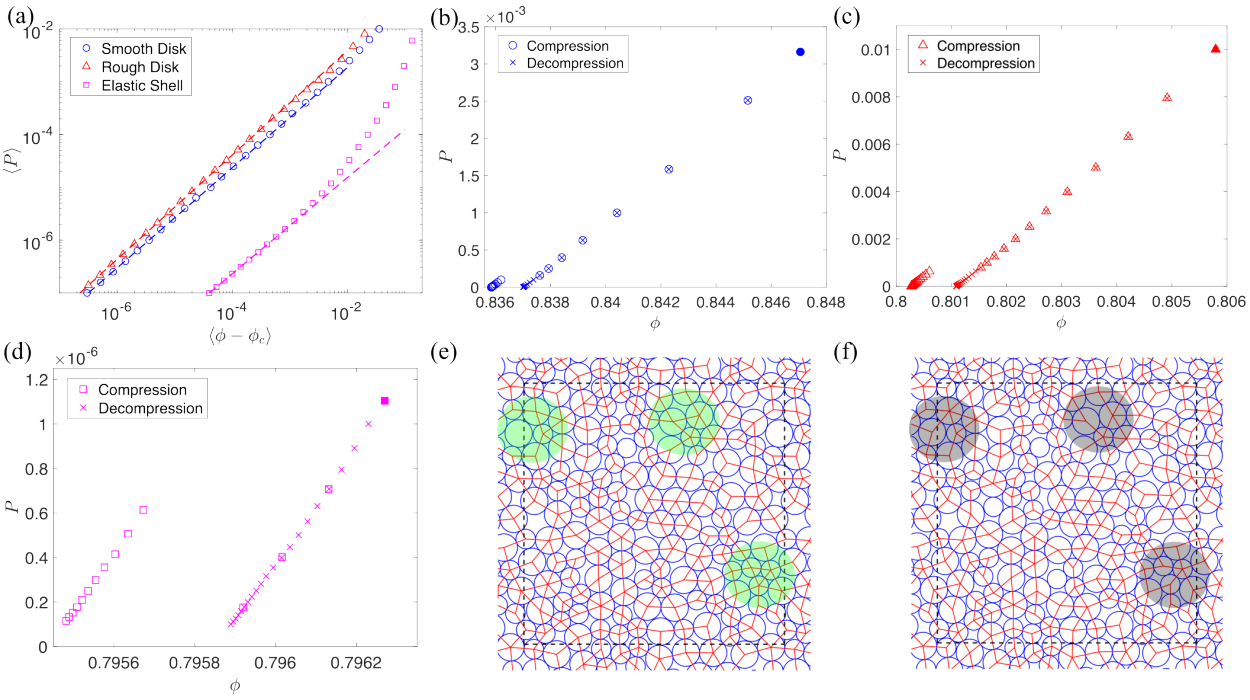

FIG. 9. (a) Ensemble-averaged pressure $\langle P \rangle$ (in units of $k_a^{2D} a_0$) versus the deviation in packing fraction $\langle \phi - \phi_c \rangle$ from jamming onset at ϕ_c during compression for $N = 128$ (a) smooth disks with purely repulsive linear spring interactions (blue circles), rough disks (red triangles), and elastic shell particles with $\mathcal{A}_0^{2D} = \mathcal{A}_{\rm min}^{2D}$, $k_a^{2D} > 0$, $k_l^{2D} > 0$, $k_b^{2D} > 0$, and $\gamma^{2D} = 0$ (magenta squares). The smooth disk packing is bidisperse with half large disks, half small disks, and diameter ratio of 1.4. The rough disk and elastic shell particle packings are also bidisperse with half large, half small, and polygon diameter ratio of 1.4. The results are averaged over 500 packings. The dashed lines show linear fits to $\langle P \rangle = B \langle \phi - \phi_c \rangle$, where $B = 0.14$, 0.36, and 10^{-3} ($\phi_c = 0.836$, 0.79, and 0.783) for smooth disks, rough disks, and elastic shells, respectively. P versus ϕ for *individual* static packings for the same systems in (a): (b) smooth disks (circles and crosses), (c) rough disks (triangles and crosses), and (d) elastic shells (squares and crosses). The circles, triangles, and squares show results for static packings compressed starting from jamming onset. The crosses show results for packings decompressed from packings that were originally compressed to the ϕ indicated by the filled symbols. Static packings of smooth disks (e) before and (f) after a rearrangement that causes a change in the contact network (indicated by red lines) following compression by $\Delta\phi \approx 10^{-5}$. The three green (before) and gray (after) regions highlight particle rearrangements.

spring potentials with periodic boundary conditions, the pressure $\langle P \rangle$ (averaged over an ensemble of packings) increases with excess packing fraction $\phi - \phi_c$ above jamming onset: $\langle P \rangle = B\langle(\phi - \phi_c)\rangle^{\zeta}$, where ϕ_c is the packing fraction at jamming onset, B is the bulk modulus, and $\zeta = 1$ [50]. (See Fig. 9 (a).) In the case of static packings of bidisperse elastic shell particles with $\mathcal{A}_0^{2D} = \mathcal{A}_{\rm min}^{2D}$, $k_a^{2D} > 0$, $k_l^{2D} > 0$, $k_b^{2D} > 0$, and $\gamma^{2D} = 0$, we also find $\langle P \rangle = B\langle \phi - \phi_c \rangle$ at small pressures as shown in Fig. 9 (a). However, at large pressures, the deformability of the elastic shell particles plays an important role and $\langle P \rangle$ increases nonlinearly with $\langle \phi - \phi_c \rangle$. To determine whether the nonlinearity is caused by the surface roughness of the particles, we also performed isotropic compression of static packings of rough disks that that do not change shape with the same number of vertices $N_\mu = 20$ as the elastic shells. Each rough disk is modeled as a regular polygon with the associated vertices that move together as a rigid body, such that the total potential energy of the packing obeys Eq. 3 [39]. For both packings of smooth and rough disks, we find linear behavior, $\langle P \rangle = B\langle \phi - \phi_c \rangle$, for the ensemble-averaged pressure versus packing fraction relation. For individual static packings, irreversible particle rearrangements occur during compression, which cause discontinuities in the pressure versus packing fraction relation as shown in Figs. 9 (b)-(d). Note that static packings before and after particle rearrangements possess different ϕ_c. The ensemble-averaged $\langle P \rangle$ versus $\langle \phi - \phi_c \rangle$ averages over the rearrangement events giving a smooth representation of the pressure versus packing fraction relation. See an example of compression-induced particle rearrangements in static packings of smooth disks in Figs. 9 (e) and (f).

C. Vibrational Density of States

The vibrational response of individual deformable particles, as well as mechanically stable packings of deformable particles, can be obtained by calculating the eigenmodes of the dynamical matrix M, which gives the second derivatives of the total potential energy U with respect to the vertex positions:

$$M_{\mu i,\beta j} = \frac{\partial^2 U}{\partial \vec{r}_{\mu i} \partial \vec{r}_{\beta j}}. \tag{29}$$

For a system with $N_{\rm dof}$ degrees of freedom, M is a $N_{\rm dof} \times N_{\rm dof}$ matrix with $N_{\rm dof}$ eigenvalues λ_k and eigenvectors $\hat{e}_k$, where k ranges from 1 to $N_{\rm dof}$ and $\hat{e}_k \cdot \hat{e}_k = 1$. We will report

[1] M. L. Manning, Essay: Collections of deformable particles present exciting challenges for soft matter and biological physics, Phys. Rev. Lett. **130**, 130002 (2023).

[2] D. B. Khismatullin, Chapter 3: The cytoskeleton and deformability of white blood cells, in *Current Topics in Membranes*, Current Topics in Membranes, Vol. 64 (Academic Press, 2009) pp. 47–111.

[3] Y. Cheng, J. D. Treado, B. F. Lonial, P. Habdas, E. R. Weeks, M. D. Shattuck, and C. S. O'Hern, Hopper flows of deformable particles, Soft Matter **18**, 8071 (2022).

[4] Y. Yuan, Z. Zeng, Y. Xing, H. Yuan, S. Zhang, W. Kob, and Y. Wang, From creep to flow: Granular materials under cyclic shear, Nat. Commun. **15**, 3866 (2024).

[5] M. Merkel and M. L. Manning, A geometrically controlled rigidity transition in a model for confluent 3d tissues, New J. Phys. **20**, 022002 (2018).

[6] E. Dressaire and A. Sauret, Clogging of microfluidic systems, Soft Matter **13**, 37 (2016).

[7] T. E. Angelini, E. Hannezo, X. Trepat, M. Marquez, J. J. Fredberg, and D. A. Weitz, Glass-like dynamics of collective cell migration, Proc. Natl. Acad. Sci. **108**, 4714 (2011).

[8] T. Lecuit and P.-F. Lenne, Cell surface mechanics and the control of cell shape, tissue patterns and morphogenesis, Nat. Rev. Mol. Cell Biol. **8**, 633 (2007).

[9] S. Stupkiewicz, M. J. Lewandowski, and J. Lengiewicz, Micromechanical analysis of friction anisotropy in rough elastic contacts, Int. J. Solids Struct. **51**, 3931 (2014).

[10] K. L. Johnson, *Contact mechanics* (Cambridge university press, 1987).

[11] W. Liu, S. Li, A. Baule, and H. A. Makse, Adhesive loose packings of small dry particles, Soft Matter **11**, 6492 (2015).

[12] M. Mailman, C. F. Schreck, C. S. O'Hern, and B. Chakraborty, Jamming in systems composed of frictionless ellipse-shaped particles, Phys. Rev. Lett. **102**, 255501 (2009).

[13] R. Kawamoto, E. Andò, G. Viggiani, and J. E. Andrade, Level set discrete element method for three-dimensional computations with triaxial case study, J. Mech. Phys. Solids **91**, 1 (2016).

[14] J. T. Clemmer, J. M. Monti, and J. B. Lechman, A soft departure from jamming: The compaction of deformable granular matter under high pressures, Soft Matter **20**, 1702 (2024).

[15] T.-L. Vu, J. Barés, S. Mora, and S. Nezamabadi, Numerical simulations of the compaction of assemblies of rubberlike particles: A quantitative comparison with experiments, Phys. Rev. E

99, 062903 (2019).

[16] S. Nezamabadi, T. H. Nguyen, J.-Y. Delenne, and F. Radjai, Modeling soft granular materials, Granul. Matter **19**, 8 (2016).

[17] D. Cantor, M. Cárdenas-Barrantes, I. Preechawuttipong, M. Renouf, and E. Azéma, Compaction model for highly deformable particle assemblies, Phys. Rev. Lett. **124**, 208003 (2020).

[18] D. J. Durian, Foam mechanics at the bubble scale, Phys. Rev. Lett. **75**, 4780 (1995).

[19] P. V. Petkov and B. P. Radoev, Statics and dynamics of capillary bridges, Colloids Surf. A **460**, 18 (2014).

[20] J. Bostwick and P. Steen, Stability of constrained capillary surfaces, Annu. Rev. Fluid Mech. **47**, 539 (2015).

[21] R. Saye and J. Sethian, Multiscale modelling of evolving foams, J. Comput. Phys. **315**, 273 (2016).

[22] K. A. Brakke, The surface evolver, Exp. Math. **1**, 141 (1992).

[23] A. Virozub, N. Haimovich, and S. Brandon, Three-dimensional simulations of liquid bridges between two cylinders: Forces, energies, and torques, Langmuir **25**, 12837 (2009).

[24] F. Andrade, H. Al-Qureshi, and D. Hotza, Measuring the plasticity of clays: A review, Appl. Clay Sci. **51**, 1 (2011).

[25] J. Richeton, S. Ahzi, K. Vecchio, F. Jiang, and R. Adharapurapu, Influence of temperature and strain rate on the mechanical behavior of three amorphous polymers: Characterization and modeling of the compressive yield stress, Int. J. Solids Struct. **43**, 2318 (2006).

[26] A. Boromand, A. Signoriello, F. Ye, C. S. O'Hern, and M. D. Shattuck, Jamming of deformable polygons, Phys. Rev. Lett. **121**, 248003 (2018).

[27] D. Wang, J. D. Treado, A. Boromand, B. Norwick, M. P. Murrell, M. D. Shattuck, and C. S. O'Hern, The structural, vibrational, and mechanical properties of jammed packings of deformable particles in three dimensions, Soft Matter **17**, 9901 (2021).

[28] J. D. Treado, D. Wang, A. Boromand, M. P. Murrell, M. D. Shattuck, and C. S. O'Hern, Bridging particle deformability and collective response in soft solids, Phys. Rev. Mater. **5**, 055605 (2021).

[29] J. D. Treado, A. B. Roddy, G. Théroux-Rancourt, L. Zhang, C. Ambrose, C. R. Brodersen, M. D. Shattuck, and C. S. O'Hern, Localized growth and remodelling drives spongy mesophyll morphogenesis, J. R. Soc. Interface **19**, 20220602 (2022).

[30] A. T. Ton, A. K. MacKeith, M. D. Shattuck, and C. S. O'Hern, Mechanical plasticity of cell membranes enhances epithelial wound closure, Phys. Rev. Res. **6**, L012036 (2024).

[31] Y. Cheng, B. F. Lonial, S. Sista, D. J. Meer, A. Hofert, E. R. Weeks, M. D. Shattuck, and C. S. O'Hern, Flow and clogging of capillary droplets (2024), arXiv:2406.13776 [physics.comp-ph].

[32] M. Arfaee, J. Kluin, and J. T. Overvelde, Modeling the behavior of elastic pouch motors, in *2023 IEEE International Conference on Soft Robotics (RoboSoft)* (2023) pp. 1–6.

[33] K. Keren, Z. Pincus, G. M. Allen, E. L. Barnhart, G. Marriott, A. Mogilner, and J. A. Theriot, Mechanism of shape determination in motile cells, Nature **453**, 475 (2008).

[34] A. Vaziri, Mechanics of highly deformed elastic shells, Thin-Walled Struct. **47**, 692 (2009).

[35] J. N. Thon, H. Macleod, A. J. Begonja, J. Zhu, K.-C. Lee, A. Mogilner, J. H. Hartwig, and J. E. Italiano, Microtubule and cortical forces determine platelet size during vascular platelet production, Nat. Commun **3**, 852 (2012).

[36] P. B. Umbanhowar, V. Prasad, and D. A. Weitz, Monodisperse Emulsion Generation via Drop Break Off in a Coflowing Stream, Langmuir **16**, 347 (2000).

[37] M. A. C. Teixeira, S. Arscott, S. J. Cox, and P. I. C. Teixeira, What is the shape of an air bubble on a liquid surface?, Langmuir **31**, 13708 (2015).

[38] Y. Zheng, D. Wang, G. Beeghly, C. Fischbach, M. D. Shattuck, and C. S. O'Hern, Computational modeling of the physical features that influence breast cancer invasion into adipose tissue, APL Bioeng. **8**, 036104 (2024).

[39] S. Papanikolaou, C. S. O'Hern, and M. D. Shattuck, Isostaticity at frictional jamming, Phys. Rev. Lett. **110**, 198002 (2013).

[40] M. Puttock and E. Thwaite, *Elastic compression of spheres and cylinders at point and line contact* (Commonwealth Scientific and Industrial Research Organization Melbourne, 1969).

[41] Y. Li, X.-L. Gao, S. Horner, and J. Zheng, Analytical models for the impact of a solid sphere on a fluid-filled spherical shell incorporating the stress wave propagation effect and their applications to blunt head impacts, Int. J. Mech. Sci. **130**, 586 (2017).

[42] E. Bitzek, P. Koskinen, F. Gähler, M. Moseler, and P. Gumbsch, Structural relaxation made simple, Phys. Rev. Lett. **97**, 170201 (2006).

[43] M. C. Fang, Closed form for half-area overlap offset of 2 unit disks (2024), arXiv:2403.10529 [math.GM].

[44] A. P. Thompson, S. J. Plimpton, and W. Mattson, General formulation of pressure and stress

tensor for arbitrary many-body interaction potentials under periodic boundary conditions, J. Chem. Phys. **131**, 154107 (2009).

[45] M. J. Louwerse and E. J. Baerends, Calculation of pressure in case of periodic boundary conditions, Chem. Phys. Lett. **421**, 138 (2006).

[46] S. Zhang, W. Jin, D. Wang, D. Xu, J. Zhang, M. D. Shattuck, and C. S. O'Hern, Local and global measures of the shear moduli of jammed disk packings, Phys. Rev. E **107**, 054903 (2023).

[47] A. I. Murdoch, A Critique of Atomistic Definitions of the Stress Tensor, J. Elast. **88**, 113 (2007).

[48] J. H. Irving and J. G. Kirkwood, The statistical mechanical theory of transport processes. IV. The equations of hydrodynamics, J. Chem. Phys. **18**, 817 (1950).

[49] K. Shi, E. R. Smith, E. E. Santiso, and K. E. Gubbins, A perspective on the microscopic pressure (stress) tensor: History, current understanding, and future challenges, J. Chem. Phys. **158**, 040901 (2023).

[50] C. S. O'Hern, L. E. Silbert, A. J. Liu, and S. R. Nagel, Jamming at zero temperature and zero applied stress: The epitome of disorder, Phys. Rev. E **68**, 011306 (2003).

[51] A. V. Tkachenko and T. A. Witten, Stress propagation through frictionless granular material, Phys. Rev. E **60**, 687 (1999).

[52] T. C. Lubensky, C. L. Kane, X. Mao, A. Souslov, and K. Sun, Corrigendum: Phonons and elasticity in critically coordinated lattices, Rep. Prog. Phys. **78**, 109501 (2015).

[53] K. VanderWerf, W. Jin, M. D. Shattuck, and C. S. O'Hern, Hypostatic jammed packings of frictionless nonspherical particles, Phys. Rev. E **97**, 012909 (2018).

[54] Y. Yuan, K. VanderWerf, M. D. Shattuck, and C. S. O'Hern, Jammed packings of 3d superellipsoids with tunable packing fraction, coordination number, and ordering, Soft Matter **15**, 9751 (2019).

[55] C. Brito, H. Ikeda, P. Urbani, M. Wyart, and F. Zamponi, Universality of jamming of nonspherical particles, Proc. Natl. Acad. Sci. **115**, 11736 (2018).

[56] M. P. Allen and D. J. Tildesley, *Computer Simulation of Liquids* (Oxford University Press, 2017).

[57] K. VanderWerf, A. Boromand, M. D. Shattuck, and C. S. O'Hern, Pressure dependent shear response of jammed packings of frictionless spherical particles, Phys. Rev. Lett. **124**, 038004

(2020).

[58] J. Zhang, D. Wang, W. Jin, A. Xia, N. Pashine, R. Kramer-Bottiglio, M. D. Shattuck, and C. S. O'Hern, Designing the pressure-dependent shear modulus using tessellated granular metamaterials, Phys. Rev. E **108**, 034901 (2023).

[59] S. Dagois-Bohy, B. P. Tighe, J. Simon, S. Henkes, and M. van Hecke, Soft-sphere packings at finite pressure but unstable to shear, Phys. Rev. Lett. **109**, 095703 (2012).